JOURNAL OF AIRCRAFT
Vol. 48, No. 1, January–February 2011

Estimating the Deployment Pressure in Pumpkin Balloons

Frank Baginski*
George Washington University, Washington, District of Columbia 20052
and
Kenneth Brakke†
Susquehanna University, Selinsgrove, Pennsylvania 17870

DOI: 10.2514/1.C031083

A vexing conundrum that has hindered the development of a high-altitude heavy-lift pumpkin balloon system is the system's ability to reliably deploy into the desired symmetric shape. With design strategies honed by empirical results from inflation tests in 2007 using 27-m-diam 200-gore pumpkin balloons, NASA's Balloon Program Office executed successful pumpkin deployments in 2008: Flight 586-NT, a 2 million cubic foot 200-gore design, and Flight 591-NT, a 6 million ft^3 200-gore design. Earlier stability analysis of strained symmetric float shapes yielded partial information regarding deployment. Balloons that were found to have a large number of unstable modes at float conditions were found also to have deployment problems. The question remained, what was the minimum pressure at which a pumpkin balloon would deploy into a cyclically symmetric shape (not necessarily the fully developed one)? Careful examination of a family of axisymmetric ascent shapes revealed a correlation between differential pressure and the number of unstable modes. In this paper, criteria that can be used to estimate the deployment pressure is presented. To bound the problem, fixed-, constrained-, and free-boundary conditions are considered for the top endplate fitting. It was found that the stability results using the fixed and constrained conditions are nearly identical, and so the strategy for estimating the deployment pressure, called the deployment pathway portrait, is as follows. The deployment pressure P_{Dep} is defined as the smallest nadir pressure where the top-free boundary condition yields two unstable modes and the top-fixed boundary condition yields no unstable modes. The approach is validated by comparing analytical predictions of deployment pressures based on the deployment pathway portrait with the deployment pressures that were recorded during the inflation tests in 2007: Flight 586-NT and Flight 591-NT. Very good agreement between the observed deployment pressures and the analytical predictions was found. This is the first analytical-based approach for estimating the deployment pressure.

Nomenclature

BA	=	bulge angle of gore (see Fig. 1)
b	=	specific buoyancy of lifting gas for ascent shape
b_d	=	specific buoyancy of lifting gas for design shape
D	=	balloon diameter
$Df(\boldsymbol{q})$	=	gradient of f with respect to degrees of freedom $\boldsymbol{q}$
f	=	total energy of balloon system
H	=	balloon height
h	=	balloon film thickness
$H_f(\boldsymbol{q})$	=	Hessian matrix of f
N	=	number of degrees of freedom in discrete complete shape $\mathcal{S}(\boldsymbol{q})$
n_g	=	number of gores
$N^-_{\mathsf{Con}}(P)$	=	number of negative eigenvalues of $H_f[\mathcal{S}(P)]$ using top-constrained boundary condition
$N^-_{\mathsf{Fix}}(P)$	=	number of negative eigenvalues of $H_f[\mathcal{S}(P)]$ using top-fixed boundary condition
$N^-_{\mathsf{Free}}(P)$	=	number of negative eigenvalues of $H_f[\mathcal{S}(P)]$ using top-free boundary condition
P_{Dep}	=	predicted deployment pressure; lowest P for which $N^-_{\mathsf{Free}}(P)$ is two and $N^-_{\mathsf{Fix}}(P)$ is zero
p_0	=	differential pressure at nadir fitting for ascent shape
$p_{0,d}$	=	differential pressure at nadir fitting for design shape
p_1	=	differential pressure at apex fitting for ascent shape
$p_{1,d}$	=	differential pressure at apex fitting for design shape
$\mathbf{q}$	=	vector of degrees of freedom $(q_1, q_2, \ldots, q_N)$
$\mathcal{S}$	=	balloon shape
S/C	=	ratio of bulge arc length to tendon-to-tendon chord length
$\mathcal{S}(P)$	=	complete balloon ascent shape with differential pressure P
$\mathcal{S}_F$	=	fundamental section, a single pumpkin lobe in a symmetric balloon shape
$V(\mathcal{S})$	=	volume of balloon shape $\mathcal{S}$
λ_{-i}	=	ith negative eigenvalue of H_f ($\lambda_{-i-1} < \lambda_{-i}$)

I. Introduction

THE pumpkin-shaped balloon offers certain advantages over axisymmetric balloon designs of comparable size because the curvature of the lobe allows the balloon designer to mitigate high film stresses. This is especially true for large scientific balloons where the balloon diameter can exceed 100 m. In a large pumpkin balloon, the bulge radius of the lobe r_B (see Fig. 1) is much smaller than the meridional radius of curvature r_M, and the corresponding hoop stress resultant is approximately $r_B P$ where P is the differential pressure. Thus, the film stress resultants in the hoop direction can be reduced by minimizing r_B. Loads are transferred from the film to strong tendons that run along the gore edges (see Fig. 1) and connect to rigid end fittings located at the balloon's apex and nadir. We assume that the nadir end fitting is fixed in the $z = 0$ plane, and we will consider three different boundary conditions (BCs) for the apex end fitting.

While the pumpkin-shape concept for a thin compliant pressure vessel goes back to Taylor in his work on parachutes [1], a number of design strategies have been proposed to achieve a pumpkin-shaped balloon [2]. The reader is referred to Fig. 1, where a schematic of a single pumpkin lobe with tendons is presented. Transverse to each longitude is a circular arc of length $BA \cdot r_B$, where the circle's bulge radius and bulge angle are denoted r_B and BA, respectively. In a

Presented as Paper 2010-2669 at the 51st AIAA/ASME/ASCE/AHS/ASC Structures, Structural Dynamics, and Materials Conference and 11th AIAA Gossamer Systems Forum, Orlando, FL, 11–15 April 2010; received 27 April 2010; revision received 24 August 2010; accepted for publication 2 September 2010.

*Professor, Department of Mathematics. Senior Member AIAA.
†Professor, Department of Mathematical Sciences.

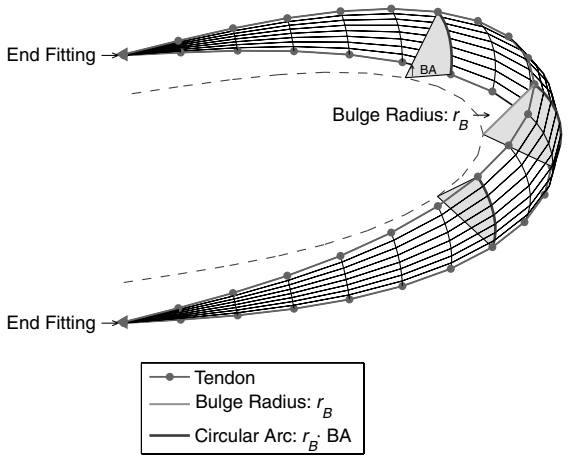

Fig. 1 Schematic of a single pumpkin lobe with tendons.

constant bulge radius design (CBR), r_B is constant along the length of the lobe and *BA* varies. In a constant bulge angle design (CBA), r_B varies along the length of the lobe and *BA* is constant. In the 1980s, Nott proposed a pumpkin balloon called *Endeavour* for circumnavigation of the Earth [3]. *Endeavour* was based on a CBA strategy, and it was one of the first pumpkin balloons to encounter deployment problems. Calledine [4] used stability to explain the behavior of *Endeavour*. While the CBR approach to pumpkin balloon design had a few successful deployments (e.g., Flight 474-NT on 23 October 1999 and Flight 485-NT on 4 June 2000), the CBR design had its own share of problems. A combination of small bulge radius and large number of gores led to unstable designs and deployment problems [5]. Excessive tendon foreshortening may have been another factor contributing to the instability of some of the early CBR designs [6]. The sensitivity of the CBA pumpkin design to the number of gores was first noted by Calledine in his stability work on *Endeavour* [4].

When a pumpkin balloon failed to deploy properly during ascent, the balloon would often take on a distinct configuration that has come to be known as an S cleft. In Fig. 2, we see S clefts in Flight 496-NT, Flight 517-NT, and Flight 555-NT. While Flights 496-NT and 517-NT were CBR designs, Flight 555-NT was a hybrid of a constant bulge angle and CBR design. Even though this hybrid design is no longer under consideration as a design approach, because of the small amount of available flight data for these size balloons, it is worth studying Flight 555-NT in order to better understand the general deployment problem. Although the Flight 555-NT gore pattern was not available, we were able to obtain the gore pattern for a one-third scale mockup of the Flight 555-NT design and include this hybrid design (BA98H) in our analysis. Since Flight 555-NT, the constant stress (CS) design developed by Farley, at the NASA Goddard Space Flight Center, has been used to design pumpkin balloons for NASA's Balloon Program Office (BPO). The CS design is incorporated into Farley's design code Planetary Balloon [7]. In the CS approach, mechanical properties of the balloon film and load tendons are used to estimate the strained shape of a pumpkin lobe under certain design conditions. The flat cutting pattern for the gore is then backed out from this strained shape. The design philosophy leads to a cutting pattern that favors deployment by keeping excess gore width to a minimum. In this paper, we will restrict our attention to CS pumpkin designs, although for comparison of deployment behavior, we consider one zero-pressure (ZP) design [2]. For the CS designs that we analyze in this paper, we use Planetary Balloon to generate the cutting pattern. We use Surface Evolver [8] to compute the strained shape of a pumpkin lobe and to carry out stability analysis of cyclically symmetric shapes.

While a number of researchers have gained some insight into the deployment problem by experiment and analysis with 3–4-m-diam pumpkin balloons [9], to capture the appropriate behavior of a balloon with over 200 gores, a significantly larger balloon was needed. This was particularly important in order to unravel the S-cleft phenomenon. To properly address these issues, the NASA BPO executed a series of inflation tests in 2007 for a class of 200 gore 27-m-diam pumpkin balloons at the TCOM Manufacturing and Test Flight Facility in Elizabeth City, North Carolina. Four test vehicles that we refer to as BA98H, BA90CS, BA55CS, and BA27CS were fabricated. BA98H (equatorial bulge angle 98 deg, hybrid design) was a one-third scale mockup of the Flight 555-NT balloon. The remaining three balloons were CS designs: BA90CS (equatorial bulge angle 90 deg), BA55CS (equatorial bulge angle 55 deg), and BA27CS (equatorial bulge angle 27 deg). BA90CS, BA55CS, and BA27CS successfully deployed during the inflation tests that mimicked ascent (see Fig. 3). The test involving BA98H reproduced the 555-NT S cleft [10] with astonishing clarity, as shown in Fig. 4.

Since the 2007 inflation tests at TCOM, there have been two successful deployments of flight balloons: Flight 586-NT launched from Fort Sumner, New Mexico in Spring 2008, and Flight 591-NT launched from Antarctica in Winter 2008 (see Fig. 5). Flight 591-NT set an endurance record by staying aloft more than 54 days. Physical dimensions, characteristics, and design parameters for Flights 586-NT and 591-NT are presented in Table 1. In Table 1, the super pressure (SP) is a 105-m-diam CS design. The ZP design is presented for comparison purposes. A constant hoop stress parameter for the CS model implemented in Planetary Balloon is σ_H. A decrease in σ_H results in a decrease in the equatorial bulge radius and an increase in the equatorial bulge angle of a gore lobe. The ZP design has a nadir cone half angle of about 60 deg and includes a 55 m 38μ cap. The cone half angle in a fully developed pumpkin balloon is nearly 90 deg. The design parameters for the 27-m-diam test vehicles BA98H, BA90CS, and BA55CS can be found in [6] (Table 2).

In Sec. II, we discuss the deployment problem and motivate our approach for estimating the deployment pressure. In Sec. III, we outline our mathematical model for determining a strained equilibrium configuration. In Sec. IV, we define the top end-fitting

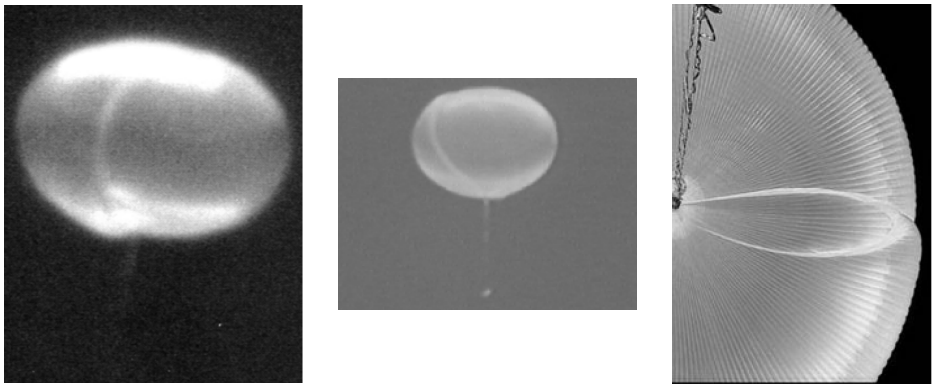

a) Flight 496-NT **b) Flight 517-NT** **c) Flight 555-NT**

Fig. 2 Flights a) 496-NT, CBR design (March 2001); b) 517-NT, CBR design (March 2003); and c) 555-NT, H design (June 2006).

a) BA27CS, deployed at $p_0 \approx 0$Pa

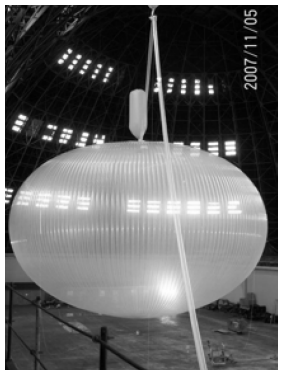

b) BA55CS, deployed at $p_0 \approx 2.5$Pa

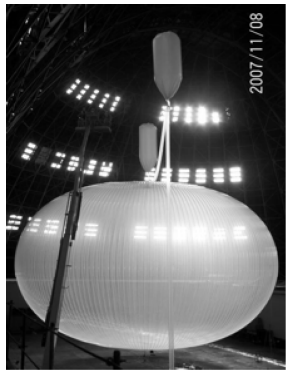

c) BA90CS, deployed at $p_0 \approx 10$Pa

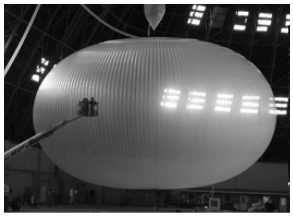

d) BA27CS, fully developed

e) BA55CS, fully developed

f) BA90CS, fully developed

Fig. 3 CS design pumpkins at deployment.

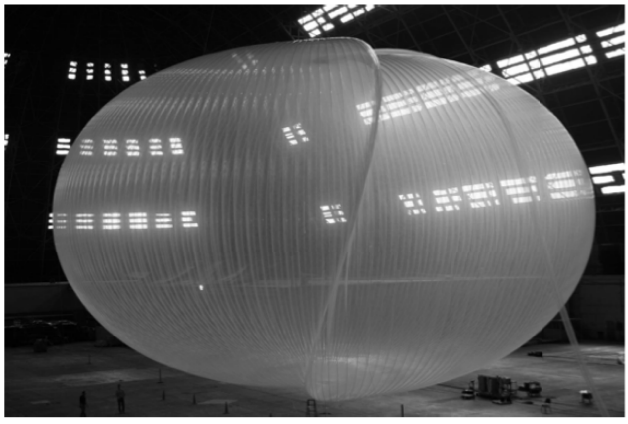

Fig. 4 One-third scale mockup of Flight 555-NT: $p_0 > 0$.

BCs that we consider in this paper. In Sec. V, we present our strategy for estimating the deployment pressure of a balloon. In Sec. VI, we calculate the deployment pathway portraits (DPPs) for the designs BA98H, BA90CS, BA55CS, BA27CS, Flight 586-NT, and Flight 591-NT, and we estimate the deployment pressure in each case. We then compare observed deployment pressures from inflation tests and flights with predictions based on the DPP approach and find good agreement between observed and predicted deployment pressures.

II. Deployment Problem

After a balloon has been released from the launch spool, it will take on a shape similar to the one displayed in Fig. 6a. In this configuration, the majority of the balloon film hangs loosely beneath a tiny gas bubble. From afar, it may appear that the balloon shape is axisymmetric, but a close examination reveals a much more complicated structure that is not symmetric. Modeling difficulties are compounded further by the fact that there are many equilibrium

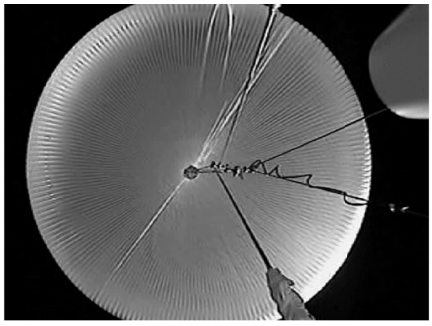

a) Flight 586-NT

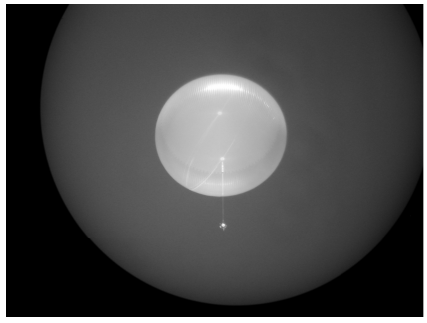

b) Flight 591-NT

Fig. 5 Deployments of a) Flight 586-NT at apex pressure 50–60 Pa (nadir pressure: 45–55 Pa) and b) Flight 591-NT at nadir pressure 10 Pa [10].

Table 1 Large scientific balloon design parameters[a]

Parameter	586-NT	591-NT	SP	ZP
Design hoop stress σ_H. MPa	4	7	8.5	NA
Diameter, m	54.47	82.541	105.831	113
Height, m	33.357	51.777	65.948	94
Film thickness, μ	38.1	38.1	38.1	38.1
Cap thickness, μ	NA	NA	38	38
Volume, m^3	56791	200691	420149	582361
Apex pressure, p_1 (Pa)	200	125	125	8.2
Nadir pressure, p_0, Pa	195.28	120.56	120.5	0
Number of gores, n_g	200	200	230	290
Equatorial bulge angle, BA, deg	55.2	26.8	37	NA
S/C	1.0397	1.0092	1.0110	NA
Equatorial bulge radius, r_B, m	0.924	2.8	2.278	NA
Design buoyancy b_d, N/m^3	0.0867	0.142	0.085	0.087
Young's moduli, MPa	152.5, 166.5	158, 162	202, 236	200
Poisson ratios	0.65, 0.75	0.6, 0.7	0.58, 0.676	0.70

[a]NA: not applicable.

configurations for the same amount of lifting gas. As a function of volume (or equivalently, nadir pressure p_0), the shape at any given moment is load-path dependent. Fabrication issues aside, for two identical tests with two identical balloons, at best, one would find shapes with similar characteristics when $V < V_d$. It is only when V approaches V_d and p_0 approaches $p_{0,d}$ that one can even begin to consider the uniqueness of the equilibrium shape.

As a balloon ascends, the volume of the lifting gas expands, and at a later time during ascent, a pumpkin balloon will assume a shape with characteristics similar to the one shown in Fig. 6b. While most of the balloon is in a deployed state, a number of longitudinal folds distributed in some asymmetric fashion about the circumference are visible. For the shape presented in Fig. 6b, the volume of the gas is roughly 50% of full capacity. There are good reasons to study offdesign configurations of the type shown in Figs. 6a and 6b, especially to investigate the presence of stress risers. However, if the film is not overstressed and the balloon ultimately deploys, these offdesign shapes are transitory and not of primary importance. If the ascent is nominal (and all goes as planned), as the balloon nears float altitude, all material will deploy and the balloon will assume the desired pumpkin shape, such as the one shown in Fig. 6c. However, there may be some mechanism at work that locks the balloon into an undesirable configuration during ascent, before coming into float. Once an offdesign shape is locked in, deployment is impossible, and so it is important to investigate balloon shapes when $p_0 \ll p_{0,d}$.

In earlier work, the authors focused on stability of the balloon at the design (float) condition $p_0 = p_{0,d}$. We noted that when the balloon properly deployed, its symmetric shape at float conditions was stable, and when the balloon did not deploy, the symmetric shape at float was found to be unstable. It should be noted that BA55CS fully deployed during testing, yet it was found to have two top-free unstable modes when $p_0 = p_{0,d}$. BA90CS fully deployed, yet it was found to have one top-fixed unstable mode and four top-free unstable modes when $p_0 = p_{0,d}$. When the symmetric equilibrium shape is unstable, there should be nearby alternate equilibrium shapes of lower energy, and this is indeed the case. Examples of such nonsymmetric equilibrium shapes associated with these instabilities are shown in Figs. 7a and 7b. The maximum total displacement from the symmetric shape was approximately 80 cm for the shape in Fig. 7a, and it was 21 cm for the shape in Fig. 7b. The three-lobe shape in Fig. 7b would have been indistinguishable with the naked eye from the symmetric shape. See [6] (Table 3) for more details on the

Table 2 BA98H DPP[a]

		Top free		Top constrained		Top fixed	
Vol. ratio, V/V_d	Nadir pressure, p_0	N^-_{Free}	Mode type	N^-_{Con}	Mode type	N^-_{Fix}	Mode type
1.000	237.000017	7	5,6,4,7,3,8,2	5	5,6,4,7,3	5	5,6,4,7,3
0.998	210.719572	7	5,4,6,3,7,2,8	5	5,4,6,3,7	5	5,4,6,3,7
0.995	184.319980	7	5,4,6,3,7,2,8	4	5,4,6,3	4	5,4,6,3
0.993	157.807406	7	5,4,6,3,7,2,8	4	5,4,6,3	4	5,4,6,3
0.990	131.195818	6	4,5,3,6,7,2	4	4,5,3,6	4	4,5,3,6
0.988	104.520204	6	4,5,3,6,2,7	3	4,5,3	3	4,5,3
0.985	77.884429	5	4,3,5,2,6	3	4,3,5	3	4,3,5
0.983	51.783430	4	4,3,5,2	2	4,3	2	4,3
0.980	28.362555	4	3,4,2,5	2	4,3	2	4,3
0.978	14.647512	4	3,4,2,5	2	3,4	2	3,4
0.975	9.444684	4	3,4,2,5	2	4,3	2	4,3
0.973	7.087866	4	3,4,2,5	2	4,3	2	4,3
0.970	5.730594	5	4,3,5,2,6	2	4,3	2	4,3
0.968	4.831647	6	4,3,5,2,6,7	3	4,3,5	3	4,3,5
0.965	4.182093	7	4,3,5,2,6,7,8	3	4,3,5	3	4,3,5
0.963	3.684564	7	4,3,5,2,6,7,8	3	4,3,5	3	4,3,5
0.960	3.287320	8	4,3,5,6,2,7,8,9	3	4,5,3	3	4,5,5
0.958	2.960162	8	4,3,5,6,7,8,2,9	3	4,5,3	3	4,5,3
0.955	2.684205	9	4,3,5,6,2,7,9,2,10	3	4,5,3	3	4,5,3
0.953	2.446971	9	4,5,3,8,6,7,9,4,10	3	4,5,3	4	4,5,3,6
0.950	2.239853	9	4,5,3,8,6,7,9,10,10	4	4,5,3,6	4	4,5,3,6
0.948	2.056705	10	4,5,3,8,9,12,7,10,2,11	4	4,5,3,6	6	4,5,3,6,2,2
0.945	1.893011	10	4,5,3,8,9,12,7,10,2,11	6	4,5,6,4,2,2	7	4,5,3,6,2,9,4
0.943	1.744461	11	Many	8	Many	9	Many

[a]One-third scale of 555-NT. S cleft formed and balloon never deployed. The k-lobe modes are presented in order of eigenvalue, most unstable first. As there is no P satisfying Eqs. (12) and (13), P_{Dep} is not defined.

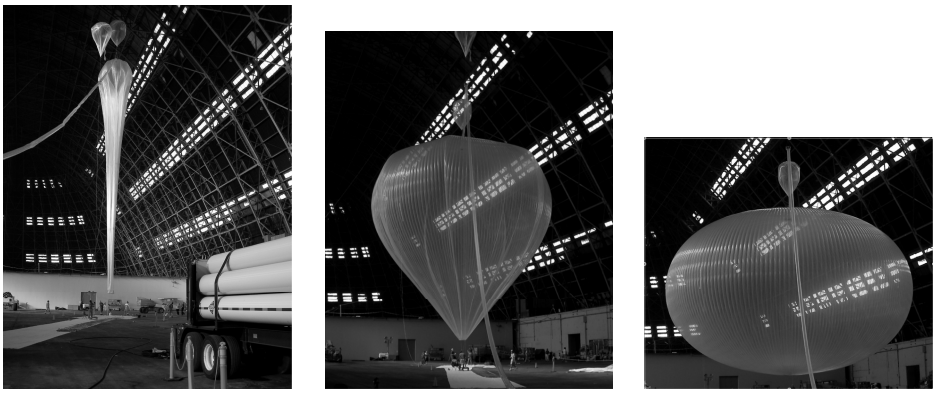

a) $V/V_d < 0.01$ b) $V/V_d \approx 0.50$ c) $V/V_d = 1.00$

Fig. 6 A family of ascent shapes: a) shortly after launch ($V/V_d < 0.01$), b) midascent ($V/V_d \approx 0.50$), and c) float shape ($V/V_d = 1.00$).

comparison of the symmetric shape and the nonsymmetric shape. When the number of unstable modes is small, one can use the eigenvector associated with a negative eigenvalue as a seed to find solutions with k-mode symmetry, as shown in Figs. 7a and 7b. However, if the number of unstable modes is large, then this is not a very efficient way to thoroughly explore the solution space. We will comment further on these issues in Sec. VI.

When standard finite element methods are applied to a wrinkled membrane, numerical difficulties arise due to the fact that the stiffness matrix is necessarily singular in the wrinkled regions. Stein and Hedgepeth [11] developed a practical approach to handle wrinkling that could be implemented into a commercial finite element code via a user-defined material subroutine [12]. Schur [13] and Liu et al. [14] were the first to apply tension field theory to balloons. Although the theory does allow for the appropriate structural response, it does not provide specific details of the wrinkling [15]. Other researchers have been able to extract these finer details, obtaining good agreement between numerical results and experiments in benchmark tests ([16], Fig. 2). The good qualitative agreement between numerical and experimental results ([15], comparison of analysis and experiment) confirms that the tension field theory properly describes the structural response of the membrane. Further advances have been developed that use sensitivity analysis to reduce the amount of wrinkling [17]. While the previously cited methods are successful when applied to a benchmark problem [15,16] or a subset of a larger structure [14], the detail of wrinkling and the folds of excess material in a complete balloon configuration, as presented in Figs. 6a and 6b, would overwhelm the capacity of most computers.

Some authors have tried to explain the deployment of pumpkin balloons by focusing on high-pressure scenarios [18]. The high pressure has the benefit of eliminating wrinkling in the balloon film, thus avoiding the problem of a singular stiffness matrix. However, it is precisely the low-pressure regime that is important to explore because of the load-path-dependent nature of offdesign shapes. The detailed features of the wrinkled structure are not of primary importance in the present work. The beauty of Pipkin's formulation of wrinkling via relaxation of the film strain energy density [19] is that it allows one to model the response of a thin membrane in these low-pressure regimes. By introducing a modified Cauchy–Green strain and a wrinkling strain [19], the stress–strain constitutive relation is well defined regardless of the local state of the membrane: slack, wrinkled, or taut ([20], Sec. 3.2). Our optimization-based solver is well suited for numerical computation, since all quantities and their first- and second-order derivatives can be explicitly calculated. This is especially useful in our stability studies, since the Hessian matrix can be assembled without the need to numerically approximate second-order derivatives.

Because we will be studying configurations for $p_0 < p_{0,d}$, it is important to distinguish between a state where the balloon is deployed and a state where the pumpkin shape is fully developed. In Figs. 3a–3c, we see BA27CS, BA55CS, and BA90CS are deployed. At this stage, the balloon is free of any longitudinal folds, all gores are deployed, and all tendons are separated, but the desired pumpkin shape is not fully developed. It is interesting to note that if a test balloon such as BA90CS, BA55CS, and BA27CS deployed, then it did so before reaching the design pressure $p_{0,d}$ but in a state where the volume was between 95–99% of capacity. However, for this small change in volume, there is significant change in geometry (see Fig. 3) and a rapid change in differential pressure. This is unlike the ascent profile of a ZP balloon, where the magnitude of the pressure is much smaller and the change in pressure as a function of altitude is much more gradual, especially as the balloon comes into float. There is little change in the geometry in a ZP balloon when the final 10% in

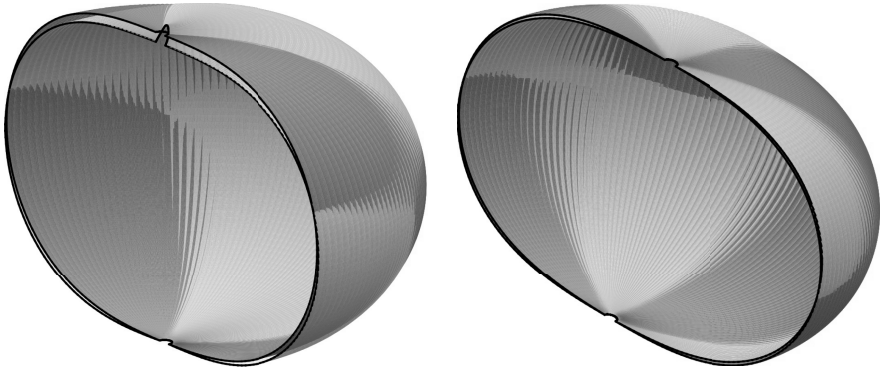

a) BA55CS (Top-Free BC) b) BA90CS (Top-Fixed BC)

Fig. 7 Asymmetric equilibria of CS designs: a) BA55CS two-lobe symmetry and b) BA90CS three-lobe symmetry. Each image is the superposition of a shaded symmetric equilibrium shape and a white lobed equilibrium shape.

volume is filled. See the last paragraph in Sec. V for a comparison of the symmetric ascent profiles of a pumpkin balloon versus a ZP balloon.

Once a balloon is deployed, it is easy for it to pressurize to the desired level and achieve the desired pumpkin shape. On the other hand, BA98H never had a chance of deploying. There were always at least two top-fixed unstable modes and four top-free unstable modes. In fact, when p_0 was on the order of 30 Pa, the S cleft was clearly locked in.

The symmetric ascent shape provides an analytical means of studying solutions that bifurcate from it. If the symmetric state is unstable, there must be nearby nonsymmetric modes of lower energy. The presence of unstable modes for nadir pressure p_0 provides the balloon opportunities to fall into nonsymmetric equilibrium. For some designs, these alternative equilibrium configurations lock in and prevent full deployment (i.e., like BA98H). For other designs (like BA55CS), these alternative equilibrium configurations are transitory.

Equilibrium balloon shapes correspond to critical points of the total energy f. The proper mathematical framework for studying the critical points of f is the Morse index, which counts the number of negative eigenvalues corresponding to a critical point of f (see Remark VI.1.). The Morse index provides a measure of the complexity of the solution space. Moreover, a large number of unstable modes is a reliable indicator of deployment problems. A low number of unstable modes seems to be an indicator that the balloon will deploy. We will quantify these results in Sec. V. While it may be virtually impossible to calculate all possible alternative configurations when there is a large number of unstable eigenmodes, it is not difficult to compute the number of unstable modes of a cyclically symmetric shape.

It is clear that typical ascent shapes of real balloons are not cyclically symmetric. However, in a successful deployment sequence, all material (including that which is stored within internal folds, as those seen in Figs. 6a and 6b) will be deployed into a symmetric configuration, before full pressurization. Finally, when the balloon is fully pressurized, it will take on the fully developed pumpkin shape. The evolution of a full pumpkin balloon from ascent shape to full deployment is a computationally intensive task. However, with an appropriate means of handling self contact, this is not impossible, and shapes with the appropriate characteristic features can be calculated. In this paper, we are not concerned with calculating specific ascent configurations. Our focus is estimating the deployment pressure.

Before we discuss our approach for estimating the deployment pressure, we first present an outline of our mathematical model and follow that with a discussion of top end-fitting BCs.

III. Mathematical Model and Stability

In this section, we outline the problem of determining the equilibrium shape of a strained balloon. Details on the model can be found in [20,21]. For a complete balloon $\mathcal{S} \subset \mathrm{IR}^3$, the reference configuration is $\Omega = \cup_{i=1}^{n_g} G_i$, where G_i is isometric to the cutting pattern G_F that is provided by the balloon designer [7]. In this case, $\mathcal{S} = \cup_{i=1}^{n_g} \mathcal{S}_i$, where $\mathcal{S}_i$ is a deformation of G_i. If we restrict our attention to cyclically symmetric shapes, then an equilibrium configuration of a fundamental gore is denoted by $\mathcal{S}_F$. We will describe our model as it applies to a complete balloon. The total potential energy f of a strained balloon $\mathcal{S}$ is

$$f = \mathcal{E}_P + \mathcal{E}_{\text{film}} + \mathcal{E}_t + \mathcal{E}_{\text{top}} + S_t^* + S_{\text{film}}^* \tag{1}$$

where

$$\mathcal{E}_P = \int_{\mathcal{D}} P(z)\,\mathrm{d}V = -\int_{\mathcal{S}} \left(\frac{1}{2}bz^2 + p_0 z\right)\mathbf{k}\cdot\mathbf{n}\,\mathrm{d}\sigma \tag{2}$$

$$\mathcal{E}_{\text{film}} = \int_{\mathcal{S}} w_f z\,\mathrm{d}A \tag{3}$$

$$\mathcal{E}_t = \sum_{i=1}^{n_g} \int_0^{L_t} \boldsymbol{\alpha}_i(S)\cdot\mathbf{k}\, w_t\,\mathrm{d}S \tag{4}$$

$$\mathcal{E}_{\text{top}} = w_{\text{top}} z_{\text{top}} \tag{5}$$

$$S_t^* = \sum_{i=1}^{n_g} \int_0^{L_t} W_t^*(\epsilon_i)\,\mathrm{d}S \tag{6}$$

$$S_{\text{film}}^* = \int_\Omega W_{\text{film}}^*\,\mathrm{d}A \tag{7}$$

where $\mathrm{d}A$ is the area measure in the lay-flat reference configuration, $\mathrm{d}S$ is the arc length as measured along a tendon in its reference configuration, $\mathcal{E}_P$ is the hydrostatic pressure potential due to the lifting gas, $\mathcal{E}_{\text{film}}$ is the gravitational potential energy of the film, $\mathcal{E}_t$ is the gravitational potential energy of the load tendons, $\mathcal{E}_{\text{top}}$ is the gravitational potential energy of the apex fitting, S_t^* is the total tendon strain energy, and S_{film}^* is the total film strain energy. For some analytical studies in this paper, we consider open balloon systems where the differential pressure is in the form $-P(z) = bz + p_0$ and p_0 is the known nadir pressure. In an open system, the volume is calculated once the equilibrium shape is known. $\mathcal{D} \subset \mathrm{IR}^3$ is the region enclosed by $\mathcal{S}$, and $\mathrm{d}V$ is volume measure in IR^3. We follow the convention that $-P(z) > 0$ means that the internal pressure is greater than the external pressure. The differential pressure at the base of the balloon is p_0, where $z = 0$, b is the specific buoyancy of the lifting gas, $\mathbf{n}$ is the outward unit normal, $\mathrm{d}\sigma$ is surface area measure in the strained balloon surface, w_f is the film weight per unit area, w_t is the tendon weight per unit length, $\boldsymbol{\alpha}_i \in \mathrm{IR}^3$ is a parametrization of a deformed tendon with reference configuration Γ_i, w_{top} is the weight of the apex fitting, and z_{top} is the height of w_{top}. The strain in the ith tendon is ϵ_i. $W_t^*(\epsilon_i)$ is the relaxed strain energy density in the ith tendon. W_{film}^* is the relaxed film strain energy density. Relaxation of the film strain energy density is a way of modeling wrinkling [19] in the balloon film and has been used in the analysis of pumpkin-shaped balloons [5,21,22]. Caps can be incorporated into the model by modifying w_f and W_f^* appropriately. In a closed system, the volume is specified via a constraint and p_0 is determined from the Lagrange multiplier corresponding to that constraint. We will consider scenarios involving closed balloon systems.

To determine a strained equilibrium balloon shape, we solve the problem,

$$\min_{\mathcal{S}\in\mathcal{H}} f(\mathcal{S}) \tag{8}$$

where $\mathcal{H}$ denotes the class of feasible balloon shapes [20]. BCs are built into $\mathcal{H}$. In Eq. (8), the continuum problem of finding an equilibrium configuration of the balloon is cast as an optimization problem. This approach is particularly well suited for the analysis of compliant structures. Surface Evolver [8] is used to calculate symmetric equilibrium shapes and to carry out the stability analysis. Even though the balloon fabric is orthotropic (see, e.g., Table 1), we average the two Young's moduli and Poisson ratios to determine a single Young's modulus and Poisson ratio, so that in effect, the balloon shell is treated as if it were isotropic. In reality, the film is not perfectly orthotropic, and the differences between the E_i and the ν_i are no more than 10%. Moreover, in the low-pressure scenarios that are of primary interest in the deployment problem, orthotropy is not a significant factor. For these reasons, we average the Young's moduli and Poisson ratios and assume the film is isotropic.

In the following, we let $V(\mathcal{S})$ denote the volume of the balloon shape $\mathcal{S}$. When p_0 is unknown but $V(\mathcal{S}) = V_0$, then we modify f in Eq. (1) as follows. Set

$$F(\mathcal{S}, \lambda) = f(\mathcal{S}) - \lambda(V(\mathcal{S}) - V_0) \tag{9}$$

and minimize $F(\lambda, \mathcal{S})$ over $(\mathcal{S}, \lambda) \in (\mathcal{H}, \mathrm{IR})$. The Lagrange multiplier for the volume constraint $V(\mathcal{S}) - V_0 = 0$ is λ. It can be shown that the value of λ for the corresponding equilibrium shape is equal to the nadir pressure p_0.

The degrees of freedom (DOFs) in a complete faceted balloon shape $\mathcal{S}$ are the x, y, and z coordinates of the nodes of triangular facets $\mathcal{T} \in \mathcal{S}$ that are free to move. Let $\boldsymbol{q} = (q_1, q_2, \ldots, q_N)$ be a list of the DOFs. Let $f(\boldsymbol{q})$ be the total energy of a faceted balloon configuration $\mathcal{S} = \mathcal{S}(\boldsymbol{q})$. $Df(\boldsymbol{q}) = [\partial f/\partial q_j]$, $j = 1, \ldots, N$, is the gradient of f evaluated at $\boldsymbol{q}$, where $\partial f/\partial q_j$ denotes partial differentiation with respect to q_j. The Hessian of f evaluated at $\boldsymbol{q}$ is the $N \times N$ matrix, $H_f(\boldsymbol{q}) = D^2 f(\boldsymbol{q}) = [\partial^2 f/\partial q_i \partial q_j]$, $i, \ j = 1, \ldots, N$. Note, after discretizing the balloon $\mathcal{S}(\boldsymbol{q})$, the quantities $f(\boldsymbol{q})$, $Df(\boldsymbol{q})$, and $H_f(\boldsymbol{q})$ are computed exactly. We are led to the following standard definition of stability.

Definition III.1: Let $\mathcal{S} = \mathcal{S}(\boldsymbol{q})$ be a solution of Eq. (8). We say $\mathcal{S}$ is stable if all the eigenvalues of $H_f(\boldsymbol{q})$ are positive. We say $\mathcal{S}$ is unstable if at least one eigenvalue of $H_f(\boldsymbol{q})$ is negative. We say that the stability of $\mathcal{S}$ is indeterminate if the lowest eigenvalue of $H_f(\boldsymbol{q})$ is zero.

In theory, the fully inflated shape should be cyclically symmetric so that the loads are distributed uniformly over the entire balloon. However, deployment (roughly the first ascent configuration free of S clefts with all load tendons clearly separated) will take place at a differential pressure P_{Dep} lower than the design value $p_{0,d}$. The focus of this paper is to outline an analytical approach to estimating P_{Dep}. Our approach will be validated with data recorded during inflation tests and balloon flights.

If we assume a priori that the strained balloon shape is cyclically symmetric, Eq. (8) can be solved for a half gore and $\mathcal{S}_F$ determined. Indeed, $\mathcal{S}_F$ is a stable local equilibrium within the class of cyclically symmetric shapes. However, within the larger class of feasible complete balloon shapes $\mathcal{H}$, the complete balloon generated by $\mathcal{S}_F$ could turn out to be unstable [5]. In previous stability work, Baginski et al. [5,21,22] and Baginski and Brakke [23] focused on conditions at float altitude, where $p_0 = p_{0,d}$. In this paper, we will extend our analysis and consider ascent-shaped families, where $0 < p_0 \leq p_{0,d}$.

In some of our earlier work, we noted that if we modeled a full balloon $\mathcal{S}$, we would obtain twice as many unstable modes than if we modeled one half a balloon and assumed reflectional symmetry about a vertical plane through the z axis. To reduce computation time, we restrict $\mathcal{H}$ to be the set of shapes that are symmetric with respect to the xz plane.

IV. Top End-Fitting Boundary Conditions

We consider three BCs for nodes that lie along the edge of the top end fitting. One BC, top fixed, refers to the case when the top end-fitting nodes are fixed and lie in the plane $z = z_1$. For the second BC, top constrained (TOPCON), the z component of the top end-fitting nodes lie in the plane $z = z_1$ plane, but the plane is free to move vertically. The corresponding x and y components are fixed. For the third BC, top free, the z component of the top end-fitting nodes are free to move vertically and independently of one another. In this case, the x and y components of end-fitting nodes are fixed. See Fig. 8 for a schematic showing the three different top end-fitting conditions. In Fig. 7a, we present an asymmetric equilibrium configuration of BA55CS with the top-free BC. In Fig. 7b, we present an asymmetric equilibrium configuration of BA90CS with the top-fixed BC.

One might argue that BC top fixed is too restrictive, and that BC top free is not restrictive enough. However, if there are no unstable top-free modes, one can assert that the symmetric equilibrium shape should be stable when the end fitting is included in the model. Likewise, if we find that the symmetric state is unstable with the restrictive top-fixed BC, then it should be unstable when a more realistic end-fitting condition is imposed. In this way, we hope to bound the stability problem. While we initially speculated that BC TOPCON would be a compromise between the top-free BC and the top-fixed BC, it turned out that the stability results were essentially the same when using top-fixed BC or TOPCON BC. For this reason, we will base our deployment pressure criterion on the top-free BC and the top-fixed BC. It would be very difficult to implement precise and realistic BCs for the region where the film and load tendons come together and attach to the end fitting. By analyzing the top-free and top-fixed conditions, we hope to bound the real problem.

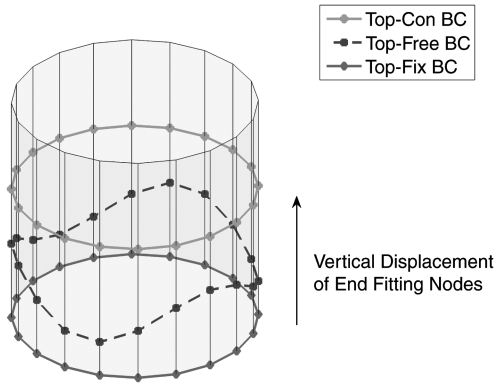

Fig. 8 Apex end-fitting BCs: top free (end-fitting nodes are free to move vertically and independently), TOPCON (end-fitting nodes are constrained to lie in a plane that can move vertically), and top fixed (end-fitting nodes are fixed).

Our numerical calculations have shown that the presence of a few top-free unstable modes is an indication of a small amount of excess material in the strained symmetric shape, and that the balloon prefers a slightly asymmetric shape that is nevertheless close to the symmetric one. For example, see Fig. 7 where a shape with two-lobe symmetry (Fig. 7a) and a shape with three-lobe symmetry (Fig. 7b) are displayed. Ideally, one would prefer a design with no unstable modes of any kind (BA27CS had zero unstable modes for $p_0 > 3.65$ Pa), but this might overly constrain the balloon designer who needs to balance the strength and weight of available materials with parameters that control the bulge angle and number of gores. Based on the available, albeit limited, flight data, a few top-free unstable modes have not proven to be detrimental to deployment. In the case of BA90CS, where four unstable top-free modes and one unstable top-fixed mode were found, the balloon deployed. Flight 586-NT (three unstable top-free modes and zero unstable top-fixed modes) also deployed. Nevertheless, it would be best to continue to gather more data on pumpkin flights as those data become available, before asserting a maximum acceptable number for the top-free BC.

V. Deployment Pathway Portrait

To mimic ascent during an inflation test like the ones carried out at TCOM in 2007, a fixed amount of helium is injected into the balloon envelope. This amount is sufficient to support the balloon. Air is then injected through an opening in the top end fitting until the desired nadir pressure level is achieved for the fully developed shape. We model this scenario by varying p_0. Occasionally, additional helium may be added in order to increase the lift or to compensate for changing atmospheric conditions. In a real ascent, one begins with a fixed amount of gas, which then expands as the balloon increases in altitude. To model this second scenario, we assume that the total lift in the balloon of volume V is fixed; that is,

$$b_d V_d = bV \tag{10}$$

Thus, in terms of the volume ratio $\tau = V/V_d$, we have

$$V = \tau V_d, \qquad b = b_d/\tau \tag{11}$$

When $0.9 < \tau < 1.0$, there is no noticeable difference in the results when using $b = b_d$ or $b = b_d/\tau$. Nevertheless, parametrizing the ascent family in terms of τ would be more realistic for ascent conditions, especially when $\tau \ll 1$. In the following, let P denote the pressure of the symmetric complete ascent shape $\mathcal{S}(P)$. Normally, $-P = bz + p_0$ and b is fixed, and so often times we will refer to a family of shapes as if parametrized by p_0.

For a shape $\mathcal{S}(P)$, $N^-_{\mathsf{Free}}(P)$ denotes the number of top-free unstable modes, $N^-_{\mathsf{Con}}(P)$ denotes the number of TOPCON unstable modes, and $N^-_{\mathsf{Fix}}(P)$ denotes the number of top-fixed unstable modes. In our examination of deployment data, we observed that a pumpkin

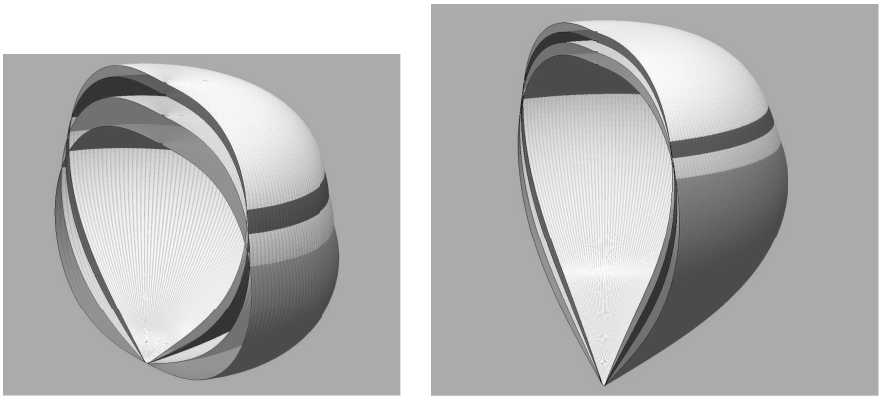

Fig. 9 Superposed symmetric ascent shape equilibria of CS design and ZP design for $\tau = 0.86, 0.90, 0.95$, and 1.0. Tallest shape corresponds to lowest τ. See Table 11 for corresponding $p_0(\tau)$.

balloon deployed at the instance when P satisfied the following two conditions:

$$N^-_{\mathsf{Free}}(P) = 2 \tag{12}$$

$$N^-_{\mathsf{Fix}}(P) = 0 \tag{13}$$

We define the deployment pressure P_{Dep} as follows:

Definition V.1.: Let $-P = bz + p_0$. The smallest nadir pressure p_0 satisfying Eqs. (12) and (13) is called the deployment pressure P_{Dep}.

In reality, the total lift in the balloon might change during the flight as a result of venting of the lifting gas, but the previous assumption is made for convenience and will suffice for our studies. If the target volume is $V_0 = \tau V_d$ in Eq. (9), we will set $b = b_d/\tau$. Thus, to compute a family of ascent shapes, we first calculate the symmetric shape for the design conditions, $b = b_d$ and $p_0 = p_{0,d}$, by solving problem (8). We define V_d to be the volume for this shape. Let

$$0 < \tau_{\min} \le \tau_1 < \tau_2 < \cdots < \tau_k \le \tau_{\max} = 1$$

For each $\tau \in \{\tau_1, \ldots, \tau_k\}$, we solve Eq. (9) to determine the symmetric equilibrium and the complete shape $\mathcal{S}(P)$ with $V = \tau V_d$ and $b = b_d/\tau$. Let $p_0(\tau)$ denote the nadir pressure for this solution. We solve the variational problem (8) with $p_0 = p_0(\tau)$ (i.e., without the volume constraint) and then carry out a stability analysis for the top-free, TOPCON, and top-fixed BCs, denoting the number of unstable modes by $N^-_{\mathsf{Free}}(P)$, $N^-_{\mathsf{Con}}(P)$, and $N^-_{\mathsf{Fix}}(P)$, respectively. The collection

$$\{[N^-_{\mathsf{Free}}(P), N^-_{\mathsf{Con}}(P), N^-_{\mathsf{Fix}}(P)], \quad -P = (b_d/\tau)z + p_0(\tau), \quad \tau_{\min} < \tau < \tau_{\max}\} \tag{14}$$

is called the DPP of the family of ascent shapes $\mathcal{S}(P)$. Once we have a DPP for a particular design, we apply Eqs. (12) and (13) to determine P_{Dep} (if it exists).

To validate the DPP approach for estimating the deployment pressure, we compare our analytical prediction with data from the TCOM tests: BA98H, BA90CS, BA55CS, and BA27CS and Flights 585-NT and 591-NT. For completeness, we determine the symmetry of each unstable mode for pressure P. A complete shape consisting of k-symmetric lobes is said to have k-lobe symmetry. Examples of two-lobe and three-lobe asymmetric equilibriums are shown in Fig. 7.

In Fig. 9a, we present ascent shapes for a pumpkin balloon for $\tau = 0.85, 0.90, 0.95$, and 1.00. A DPP of the SP design indicates a deployment pressure $P_{\mathsf{Dep}} = 6.33$ Pa, where $\tau = 0.964$. The ZP balloon design has a stellar track record of reliable deployment accumulated over decades. For this reason, we calculated a DPP for the 290 gore 113-m-diam ZP design, with characteristics as presented in Table 1. In Fig. 9b, we present symmetric ascent shapes of this design for $\tau = 0.865, 0.904, 0.952$, and 1.00.

VI. Summary and Discussion of Deployment Pathway Portrait Results

We computed DPPs for the balloon designs BA98H, BA90CS, BA55CS, BA27CS, Flight 586-NT, and Flight 591-NT. For each of these designs, we calculate the number of unstable modes for the top-free, TOPCON, and top-fixed BCs. These results are summarized in

Table 3 BA90CS DPP[a]

		Top free		Top constrained		Top fixed	
Vol. ratio, V/V_d	Nadir pressure, p_0	N^-_{Free}	Mode type	N^-_{Con}	Mode type	N^-_{Fix}	Mode type
1.000	86.000020	4	3,4,2,5	1	3	1	3
0.997	55.305683	3	3,4,2	0	——	0	——
0.994	26.636599	3	3,2,4	0	——	0	——
0.991	10.686972	3	3,2,4	0	——	0	——
0.988	6.349840	3	3,2,4	0	——	0	——
0.985	4.629958	3	3,4,2	0	——	0	——
0.982	3.679461	4	3,4,2,5	1	3	1	3
0.979	3.057410	4	3,4,2,5	2	3,4	2	3,4
0.976	2.609328	4	3,4,2,5	2	4,3	2	4,3
0.973	2.266060	6	3,4,5,2,6,7	2	4,3	2	4,3
0.970	1.991597	7	4,3,5,4,6,7,6	2	4,3	2	4,3
0.967	1.765028	8	4,3,5,6,6,7,8,9	3	4,3,5	3	4,3,5
0.964	1.573273	8	4,3,5,6,7,8,4,9	3	4,5,3	3	4,5,3
0.961	1.407716	9	4,3,5,6,8,7,9,2,10	3	4,5,3	3	4,5,3
0.958	1.262467	29	Many	22	Many	22	Many

[a]The k-lobe modes are presented in order of eigenvalue, most unstable first, deployed at around 10 Pa (nadir pressure) [10]. As there is no P satisfying Eqs. (12) and (13), P_{Dep} is not defined.

Table 4 BA55CS DPP[a]

		Top free		Top constrained		Top fixed	
Vol. ratio, V/V_d	Nadir pressure, p_0	N^-_{Free}	Mode type	N^-_{Con}	Mode type	N^-_{Fix}	Mode type
1.000	50.000017	2	2,3	0	——	0	——
0.997	22.100365	1	2	0	——	0	——
0.994	9.014477	1	2	0	——	0	——
0.991	5.641353	2	2,3	0	——	0	——
0.988	4.193140	2	3,2	0	——	0	——
0.985	3.359250	2	3,2	0	——	0	——
0.982	2.802431	2	3,2	0	——	0	——
0.979	2.396513	3	3,2,4	0	——	0	——
0.976	2.082551	3	3,2,4	0	——	0	——
0.973	1.829693	3	3,2,4	0	——	0	——
0.970	1.619754	3	3,4,2	0	——	0	——
0.967	1.441433	3	3,4,2	0	——	0	——
0.964	1.287129	4	3,4,2,5	0	——	0	——
0.961	1.151585	4	3,4,2,5	0	——	0	——
0.958	1.031023	4	3,4,2,5	0	——	0	——
0.955	0.922640	4	3,4,5,4	0	——	0	——
0.952	0.824308	5	4,3,5,4,6	1	2	1	2
0.949	0.734375	5	4,3,5,2,6	1	2	1	2
0.946	0.651554	5	4,3,5,2,6	1	2	1	2
0.943	0.574812	6	4,3,5,6,2,7	2	4,2	2	4,2
0.940	0.503317	6	4,3,5,6,2,7	2	4,2	2	4,2
0.937	0.436394	6	4,3,5,6,2,7	2	4,2	2	4,2
0.934	0.373475	6	4,5,3,6,2,7	3	5,4,4	3	5,4,4
0.931	0.314021	22	Many	18	Many	18	Many

[a]The k-lobe modes are presented in order of eigenvalue, most unstable first, deployed at around 2.5 Pa (nadir pressure) [10]. We estimate $P_{\text{Dep}} = 2.8$ Pa.

Tables 2–7. In each table, the k-lobe modes are presented in order of eigenvalue, with the most unstable first. In this section, we discuss the contents of the DPPs presented in Tables 2–7. Since there is little difference between the stability results for TOPCON and top fixed, we will restrict our discussion to the top-free and top-fixed BCs.

1) In hindsight, it is clear that BA98H was a poor design that had no hope of deploying at any pressure. For all P considered in Table 2, there are at least two top-fixed unstable modes and four top-free unstable modes. At the design pressure $p_{0,d} = 237$ Pa, there are five top-fixed unstable modes and seven top-free unstable modes.

2) Based on the DPP presented in Table 3, one would surmise that BA90CS is a borderline unacceptable design. At $p_{0,d} = 83.6$ Pa, $N^-_{\text{Free}} = 4$ and $N^-_{\text{Fix}} = 1$. For larger pressures, the number of unstable modes increase; that is, if $p_0 = 100$ Pa, then $N^-_{\text{Free}} = 4$ and $N^-_{\text{Fix}} = 2$, and if $p_0 = 200$ Pa, then $N^-_{\text{Free}} = 5$ and $N^-_{\text{Fix}} = 3$. Nevertheless, the balloon was observed to have deployed at $p_0 = 10$ Pa [10]. Even though the deployment pressure for BA90CS does not satisfy Eqs. (12) and (13), our criterion is consistent with the observed deployment pressure; that is, $N^-_{\text{Free}} = 3$ and $N^-_{\text{Fix}} = 0$ when $p_0 = 10.6$ Pa. However, in this case, we conclude that P_{Dep} is not defined.

Table 5 BA27CS DPP[a]

		Top free		Top constrained		Top fixed	
Vol. ratio, V/V_d	Nadir pressure, p_0	N^-_{Free}	Mode type	N^-_{Con}	Mode type	N^-_{Fix}	Mode type
1.000	50.000017	0	——	0	——	0	——
0.995	13.234771	0	——	0	——	0	——
0.990	5.556370	0	——	0	——	0	——
0.985	3.658673	0	——	0	——	0	——
0.980	2.739338	1	2	0	——	0	——
0.975	2.167764	1	2	0	——	0	——
0.970	1.766250	2	2,3	0	——	0	——
0.965	1.462175	2	2,3	0	——	0	——
0.960	1.220059	2	3,2	0	——	0	——
0.955	1.020237	2	3,2	0	——	0	——
0.950	0.850796	2	3,2	0	——	0	——
0.945	0.704043	3	3,2,4	0	——	0	——
0.940	0.574759	3	3,4,2	0	——	0	——
0.935	0.459259	3	3,4,2	0	——	0	——
0.930	0.354853	3	3,4,2	0	——	0	——
0.925	0.259525	4	6,4,2,5	0	——	0	——
0.920	0.171731	4	6,4,2,5	0	——	0	——
0.915	0.090254	4	6,4,5,2	0	——	0	——
0.910	0.014145	4	4,6,5,2	0	——	0	——
0.905	−0.057362	5	4,6,5,2,6	0	——	0	——
0.900	−0.124934	5	4,6,5,2,6	0	——	0	——
0.895	−0.188902	5	4,3,5,6,2	0	——	0	——
0.890	−0.249808	5	4,3,5,6,4	1	2	1	2
0.885	−0.307948	247	Many	243	Many	243	Many

[a]The k-lobe modes are presented in order of eigenvalue, most unstable first, deployed at around 0 Pa (nadir pressure) [10]. We estimate $P_{\text{Dep}} = 0.85$ Pa.

Table 6 Flight 586-NT DPP[a]

		Top free		Top constrained		Top fixed	
Vol. ratio, V/V_d	Nadir pressure, p_0	N_{Free}^-	Mode type	N_{Con}^-	Mode type	N_{Fix}^-	Mode type
1.000	195.200093	3	3,2,4	0	——	0	——
0.999	178.740752	3	3,2,4	0	——	0	——
0.998	162.263729	3	3,2,4	0	——	0	——
0.997	145.778500	3	3,2,4	0	——	0	——
0.996	129.352154	2	3,2	0	——	0	——
0.995	112.983474	2	3,2	0	——	0	——
0.994	96.690221	2	3,2	0	——	0	——
0.993	80.532280	2	3,2	0	——	0	——
0.992	64.671201	2	3,2	0	——	0	——
0.991	49.812289	2	3,2	0	——	0	——
0.990	37.054644	2	3,2	0	——	0	——
0.989	27.076785	3	3,2,4	0	——	0	——
0.988	20.377199	3	3,2,4	0	——	0	——
0.987	16.189276	3	3,2,4	1	3	1	3
0.986	13.482485	3	3,4,2	1	3	1	3
0.985	11.603788	4	3,4,2,5	2	3,4	2	3,4
0.984	10.222418	4	3,4,2,5	2	3,4	2	3,4
0.983	9.159596	4	3,4,2,5	2	3,4	2	3,4
0.982	8.310500	6	3,4,2,5,6,7	2	4,3	2	4,3
0.981	7.610386	7	4,3,5,2,6,7,8	2	4,3	2	4,3
0.980	7.018252	8	4,3,5,6,7,6,8,9	3	4,3,5	3	4,3,5
0.979	6.507522	9	4,3,5,8,7,6,6,9,10	3	4,3,5	3	4,3,5
0.978	6.060330	10	4,3,5,8,7,9,6,10,10,11	6	4,3,5,2,2,8	7	4,3,5,9,8,8,4
0.977	5.664170	13	Many	10	Many	12	Many

[a]; The k-lobe modes are presented in order of eigenvalue, most unstable first, deployed between 50–60 Pa (apex pressure) [10]. We estimate the corresponding nadir pressure is between 45–55 Pa $P_{\text{Dep}} = 37.05$ Pa.

3) From Table 4, we see BA55CS satisfies Eqs. (12) and (13) at $P_{\text{Dep}} = 2.8$ Pa, compared with the observed deployment pressure of 2.5 Pa [10]. BA55CS was a half-scale mockup of the Flight 586-NT balloon, which deployed at between 45 and 55 Pa (nadir pressure).

4) From Table 5, BA27CS satisfies Eqs. (12) and (13) at $P_{\text{Dep}} = 0.85$ Pa, compared with the observed deployment pressure of approximately 0.0 Pa [10].

5) Flight 586-NT deployed at an observed pressure between 45 and 55 Pa [10]. From Table 6, we see that the 586-NT balloon satisfies Eqs. (12) and (13) with $P_{\text{Dep}} = 37.05$ Pa.

6) Flight 591-NT deployed at an observed pressure of 10 Pa [10]. From Table 7, we see that 591-NT balloon satisfies Eqs. (12) and (13) with $P_{\text{Dep}} = 7.37$ Pa.

7) In Table 8, we present the DPP for the ZP design in Table 1. We found $P_{\text{Dep}} = -2.98$ Pa.

8) In Table 9, we present the DPP for the SP design in Table 1. We found $P_{\text{Dep}} = 6.33$ Pa.

A comparison of predicted deployment pressures and observed deployment pressures is summarized in Table 10.

Pressure gauges were located at the nadir for the inflation tests. Pressure gauges were located at the nadir for Flight 591-NT and at the apex for Flight 586-NT. To be consistent, we presented nadir pressures values in Tables 2–7 using the observed deployment pressure, the height of the balloon, and the buoyancy to estimate the nadir pressure for Flight 586-NT. Given the limited accuracy ($\approx \pm 5$ Pa) of the pressure gauges on flight balloons, the analytical predictions based on the deployment pressure criteria in Eqs. (12)

Table 7 Antarctica 2008–2009: Flight 591-NT DPP[a]

		Top free		Top constrained		Top fixed	
Vol. ratio, V/V_d	Nadir pressure, p_0	N_{Free}^-	Mode type	N_{Con}^-	Mode type	N_{Fix}^-	Mode type
1.000	120.500048	1	2	0	——	0	——
0.997	99.077402	1	2	0	——	0	——
0.994	77.628582	1	2	0	——	0	——
0.991	56.314382	1	2	0	——	0	——
0.988	35.839996	1	2	0	——	0	——
0.985	19.196269	1	2	0	——	0	——
0.982	10.893319	2	2,3	0	——	0	——
0.979	7.378377	2	3,4	0	——	0	——
0.976	5.568984	3	3,2,4	0	——	0	——
0.973	4.451831	3	3,4,4	0	——	0	——
0.970	3.677756	3	3,4,4	0	——	0	——
0.967	3.100361	4	3,4,2,5	1	3	1	3
0.964	2.647271	4	3,4,2,5	2	3,4	2	3,4
0.961	2.278320	4	3,4,5,2	2	4,3	2	4,3
0.958	1.969207	5	4,3,5,2,6	2	4,3	2	4,3
0.955	1.704315	6	4,3,5,2,6,7	3	4,3,5	3	4,3
0.952	1.473160	6	4,3,5,6,2,7	3	4,5,3	3	4,5,3
0.949	1.268451	8	4,3,5,6,2,7,8,2	4	4,5,3,6	4	4,5,3,6
0.946	1.084962	9	4,5,3,6,7,2,8,9,2	4	4,5,3,6	4	4,5,3,6
0.943	0.918824	10	4,5,3,6,7,8,2,9,10,2	5	4,5,6,3,7	5	4,5,6,3,7
0.940	0.767112	10	4,5,3,6,7,8,9,2,10,2	5	4,5,6,3,7	5	4,5,6,3,7

[a]The k-lobe modes are presented in order of eigenvalue, most unstable first, deployed at 10 Pa (nadir pressure) [10]. $P_{\text{Dep}} = 7.37$ Pa.

Table 8 DPP for a ZP balloon[a]

		Top free		Top constrained		Top fixed	
Vol. ratio, V/V_d	Nadir pressure, p_0	N^-_{Free}	Mode type	N^-_{Con}	Mode type	N^-_{Fix}	Mode type
1.000[b]	0.000000	0	——	0	——	0	——
0.975	−0.798457	0	——	0	——	0	——
0.950[b]	−1.403369	0	——	0	——	0	——
0.925	−1.925590	0	——	0	——	0	——
0.900[b]	−2.401038	0	——	0	——	0	——
0.875	−2.848719	0	——	0	——	0	——
0.8675	−2.979522	0	——	0	——	0	——
0.867344	−2.982234	0	——	0	——	0	——
0.867188	−2.984946	4	6,6,2,2	4	6,6,2,2	4	6,6,2,2
0.866875	−2.990368	6	8,8,2,2,4,4	6	8,8,2,2,4,4	6	8,8,2,2,4,4
0.86625	−3.001206	10	2,2,2,2,4,4,6,6,8,8	10	2,2,2,2,4,4,6,6,8,8	10	2,2,2,2,4,4,6,6,8,8
0.8650[b]	−3.022858	14	Many	14	Many	14	Many
0.8638	−3.043615	17	Many	17	Many	17	Many

[a]The k-lobe modes are presented in order of eigenvalue, most unstable first. $P_{\text{Dep}} = -2.84$ Pa.
[b]Corresponding symmetric ascent shape is shown in Fig. 9b.

and (13) and the observed deployment pressures are in good agreement. Unfortunately, there are sparse flight data for pumpkin balloons, and it would be desirable to carry out additional analyses to further validate the DPP approach.

It is important to note that BA55CS was a half-scale mockup of the Flight 586-NT design. While it would be impossible to scale all critical parameters precisely, our DPP approach was able to accurately predict the deployment pressure for the 27-m-diam test vehicle BA55CS and the 54-m-diam flight vehicle (586-NT). Both predictions were in good agreement with observed deployment pressures.

Note that for most of the CS pumpkin shapes considered here, the number of unstable modes decreases as $p_0 \to p_{0,d}$. The notable exceptions are BA90CS (top free, TOPCON, or top fixed), BA55CS (top free), and 586-NT (top free). Unlike the load-path-dependent indeterminate low-volume shapes, such as those is Figs. 6a and 6b, the behavior of equilibrium shapes for $p_0 > p_{0,d}$ is more akin to buckling modes in shell problems. It may be possible to show under certain conditions that a nonsymmetric shape, like the one in Fig. 7b, bifurcates from the well-defined fully developed symmetric pumpkin shape. In the same sense, other solutions may bifurcate from the symmetric shape for values of p_0 significantly less than $p_{0,d}$. When the number of negative eigenvalues of H_f is small (say, one or two), the structure of the solution space is not too complicated, and it is not difficult to calculate solutions with k-lobe symmetry. One uses a multiple of the eigenvector corresponding to a negative eigenvalue of H_f as a seed to start the solution process. Moreover, one could use a parameter such as p_0 to generate a curve of solutions with k-lobe symmetry. However, when there are m unstable eigenmodes, the solution space in a neighborhood of the asymmetric shape could be an m-dimensional manifold. If m is large, it would be extremely difficult to fully understand the nature of this manifold by studying only solutions with k-lobe symmetry. For example, the S cleft does not have k-lobe symmetry for any value of k.

Remark VI.1.. The mathematical framework for studying the critical points of functionals like f is the Morse theory or the Ljusternik–Schnirelman theory [24] and provides the rationale for counting the number of unstable eigenvalues of H_f and using Eqs. (12) and (13) as design criterion. If $\boldsymbol{q} \in \text{IR}^N$ is a critical point of f: $\text{IR}^N \to \text{IR}$, then under suitable conditions on f, the integer m

Table 9 SP pumpkin ($D = 105.8$ m, $p_1 = 125$ Pa)[a]

		Top free		Top constrained		Top fixed	
Vol. ratio, V/V_d	Nadir pressure, p_0	N^-_{Free}	Mode type	N^-_{Con}	Mode type	N^-_{Fix}	Mode type
1.000[b]	120.500029	2	2,3	0	——	0	——
0.994	90.660177	1	2	0	——	0	——
0.988	61.003254	1	2	0	——	0	——
0.982	33.434228	1	2	0	——	0	——
0.976	15.752594	2	4,3	0	——	0	——
0.970	9.167367	2	3,4	0	——	0	——
0.964	6.338192	2	3,4	0	——	0	——
0.958	4.736133	3	3,4,4	0	——	0	——
0.952[b]	3.673468	3	3,2,4	0	——	0	——
0.946	2.899362	3	3,4,2	0	——	0	——
0.940	2.299159	4	3,4,2,5	0	——	0	——
0.934	1.812768	4	3,4,2,5	0	——	0	——
0.928	1.405527	4	3,4,2,5	1	2	1	2
0.922	1.055898	4	4,3,5,2	1	2	1	2
0.916	0.749711	4	4,3,5,2	1	2	1	2
0.910	0.477196	4	4,3,5,2	1	2	1	2
0.904[b]	0.231374	5	4,3,5,2,6	1	2	1	2
0.898	0.007102	5	4,3,5,2,6	2	4,2	2	4,2
0.892	−0.199485	5	4,3,5,2,6	2	2,2	2	4,2
0.886	−0.391339	5	4,5,3,6,2	2	2,2	2	4,2
0.880	−0.570735	5	4,5,3,6,2	2	4,2	2	2,2
0.874	−0.739500	5	4,5,3,6,2	2	4,2	2	2,2
0.868	−0.900174	6	4,5,3,6,2,7	2	4,2	2	4,2
0.865[b]	−0.975794	121	Too many	117	Many	117	Many

[a]The k-lobe modes are presented in order of eigenvalue, most unstable first. $P_{\text{Dep}} = 6.33$ Pa.
[b]Corresponding symmetric ascent shape is shown in Fig. 9a.

Table 10 Predicted versus observed deployment pressures for 27-m-diam test vehicles and flight size balloons[a]

Design	V/V_d	$p_{0,d}$, Pa	Observed P_{Dep}, Pa	Predicted P_{Dep}, Pa
BA98H	ND	235	None	ND
BA90CS	ND	83.6	10	ND
BA55CS	0.982	47.6	2.5	2.8
BA27CS	0.950	47.6	0	0.8
586-NT	0.990	195	47.5	37.05
591-NT	0.979	120	10	7.37
SP	0.964	120	NA	6.38
ZP	0.875	0	NA	−2.84

[a]NA: not available; ND: not defined.

Table 11 A comparison of $p_0(\tau)$ for a ZP balloon versus a SP balloon (pumpkin)

τ	0.86	0.90	0.95	1.00
SP $p_0(\tau)$	−0.97	0.23	90.6	120.5
ZP $p_0(\tau)$	−3.10	−2.40	−1.40	0.0

equal to the number of negative eigenvalues of H_f is called the Morse index of $\boldsymbol{q}$. The critical value of f at $\boldsymbol{q}$ is called $f(\boldsymbol{q})$. If $H_f(\boldsymbol{q})$ is nonsingular, then it is a nondegenerate critical point of f. In this case, the well-known Morse Lemma states there are local coordinates $\boldsymbol{x} = (x_1, x_2, \ldots, x_N)$ and an integer m, such that $0 \le m \le N$ and f has the normal form

$$f(\boldsymbol{q}+\boldsymbol{x}) = -x_1^2 - x_2^2 - \cdots - x_m^2 + x_{m+1}^2 + x_{m+2}^2 + \cdots + x_N^2 + f(\boldsymbol{q})$$

for an $\boldsymbol{x}$ sufficiently small (see [25], Secs. 2.11–2.12).

Equations (12) and (13) provide the balloon designer with guidance and analytical ground truth for making rational design choices. Take the 591-NT design, for example. Knowing a priori that there are no alternative equilibrium configurations near the symmetric shape based on the top-fixed and TOPCON BCs is strong evidence that the balloon will deploy well before coming into float. Equations (12) and (13) provide an estimate when deployment should occur. If less restrictive BCs are placed on the top end fitting, at most, one unstable top-free mode is present and the manifold of solutions is tractable via numerical computation (it is a curve of solutions with two-lobe symmetry).

The ZP balloons have a long history of reliable deployment and, even though we did not have records of deployment pressures to validate our deployment pressure prediction, it is interesting to see how the DPP for a ZP natural shape balloon differs from that of a pumpkin balloon. The authors investigated ascent shapes of the ZP balloon in an earlier paper [26]. Geometrically, the target shape of a pumpkin balloon is more like an oblate spheroid, while the ZP balloon is more like an inverted onion. At a volume ratio of $\tau = 0.90$, the ZP balloon is very close to the fully developed target float shape (the balloon height needs to decrease another 4 m). On the other hand, at about $\tau = 0.90$, the SP design is not close to the fully developed symmetric pumpkin (the balloon height needs to decrease over 12 m). We also noted that the magnitude of the negative eigenvalues for the ZP balloon at $\tau = 0.867344$ was very small; that is, λ_{-4} was roughly 10^{-3}. Although this paper focused solely on balloons, the general stability approach to analyzing a desired equilibrium configuration should be amenable to other lightweight structures, including, for example, a tension cone inflatable aerodynamic decelerator [27,28].

VII. Conclusions

In this paper, an analytical method for estimating the deployment pressure of a pumpkin balloon was proposed. The technique requires one to carry out two types of stability analyses for a family of symmetric ascent shapes and determine its DPP. From the DPP, the lowest pressure for which the ascent shape has two unstable top-free modes and zero unstable top-fixed modes was found. The lowest pressure satisfying this criteria is defined to be the deployment pressure. This approach was validated by comparing analytical predictions with deployment pressures recorded for four inflation tests and two flight balloons. When the predicted deployment pressures were compared with the observed deployment pressures, very good agreement was found.

Acknowledgments

The authors would like to thank David Pierce, Chief of the NASA Balloon Program Office (BPO), for the opportunity to collaborate with the BPO Super Pressure Team. The first author would like to give special thanks to Rodger Farley of NASA Goddard Space Flight Center for his assistance in the use of Planetary Balloon and his insights into pumpkin balloon design. The authors thank the NASA BPO for the use of their photographs.

References

[1] Taylor, G. I., "On the Shapes of Parachutes: Paper Written for the Advisory Committee on Aeronautics, 1919," *The Scientific Papers of G. I. Taylor: Aerodynamics and the Mechanics of Projectiles and Explosions*, edited by G. K. Batchelor, Vol. 3, Cambridge Univ. Press, Cambridge, England, U. K., 1963, pp. 26–37.

[2] Baginski, F., "On the Design and Analysis of Inflated Membranes: Natural and Pumpkin Shaped Balloons," *SIAM Journal on Applied Mathematics*, Vol. 65, No. 3, 2005, pp. 838–857. doi:10.1137/S0036139903438478

[3] Nott, J., "Design Considerations and Practical Results with Long Duration Systems for Manned World Flights," *Advances in Space Research*, Vol. 33, No. 10, 2004, pp. 1667–1673. doi:10.1016/j.asr.2003.07.038

[4] Calledine, C. R., *Stability of the Endeavour Balloon, Buckling of Structures*, edited by I. Elishakoff, J. Arbocz, C. D. Babcock, Jr., and A. Libai, Elsevier, New York, 1988, pp. 133–149.

[5] Baginski, F., Brakke, K., and Schur, W., "Stability of Cyclically Symmetric Strained Pumpkin Balloon Configurations and the Formation of Undesired Equilibria," *Journal of Aircraft*, Vol. 43, No. 5, 2006, pp. 1414–1423. doi:10.2514/1.21514

[6] Baginski, F., and Brakke, K., *Exploring the Stability Landscape of Constant Stress Pumpkin Balloon Designs*, *Journal of Aircraft*, Vol. 47, No. 3, 2010, pp. 849–857. doi:10.2514/1.45497

[7] Farley, R., "Planetary Balloon: Balloon Design Software Manual," NASA Goddard Space Flight Center, Greenbelt, MD, 2007.

[8] Brakke, K., "The Surface Evolver," *Experimental Mathematics*, Vol. 1, No. 2, 1992, pp. 141–165.

[9] Schur, W. W., and Jenkins, C. H., "Deployment Destiny, Stable Equilibria, and the Implications for Gossamer Design," 43nd AIAA/ASME/ ASCE/AHS/ASC Structures, Structural Dynamics and Materials Conference and Exhibit, Denver, CO, AIAA Paper 2002-1205, 2002.

[10] Cathey, H., "The NASA Super Pressure Balloon: A Path to Flight," *Advances in Space Research*, Vol. 44, No. 1, 2009, pp 23–28. doi:10.1016/j.asr.2009.02.013

[11] Stein, M., and Hedgepeth, J. M., "Analysis of Partly Wrinkled Membranes," NASA TN D-813, July 1961.

[12] Miller, R. K., and Hedgepeth, J. M., "Algorithm for Finite Element Analysis of Partly Wrinkled Membrane Structures," *AIAA Journal*, Vol. 20, No. 12, 1982, pp. 1761–1763. doi:10.2514/3.8018

[13] Schur, W. W., "Development of a Practical Tension Field Material Model for Thin Films," *32nd Aerospace Sciences Meeting and Exhibit*, Reno, NV, AIAA Paper 1994-636, 10–13 Jan. 1994.

[14] Liu, X., Jenkins, C. H., and Schur, W. W., "Schur, Large Deflection Analysis of Pneumatic Envelopes Using a Penalty Parameter Modified Material Model," *Finite Elements in Analysis and Design*, Vol. 37, No. 3, March 2001, pp. 233–251. doi:10.1016/S0168-874X(00)00040-8

[15] Blandino, J. R., Johnston, J. D., and Dharamsi, U. K., "Corner Wrinkling of a Square Membrane due to Symmetric Mechanical Loads," *Journal of Spacecraft and Rockets*, Vol. 39, No. 5, 2002, pp. 717–724.

doi:10.2514/2.3870
[16] Tessler, A., Sleight, D. W., and Wang, J. T., "Effective Modeling and Nonlinear Shell Analysis of Thin Membranes Exhibiting Structural Wrinkling," *Journal of Spacecraft and Rockets*, Vol. 42, No. 2, 2005, pp. 287–298.
doi:10.2514/1.3915
[17] Akita, T., and Natori, M. C., "Sensitivity Analysis Method for Membrane Wrinkling Based on the Tension-Field Theory," *AIAA Journal*, Vol. 46, No. 6, 2008, pp. 1516–1527.
doi:10.2514/1.33187
[18] Pagitz, M., and Pellegrino, S., "Buckling Pressure of Pumpkin Balloons," *International Journal of Solids and Structures*, Vol. 44, No. 21, 2007, pp. 6963–6986.
doi:10.1016/j.ijsolstr.2007.03.021
[19] Pipkin, A. C., "Relaxed Energy Densities for Large Deformations of Membranes," *IMA Journal of Applied Mathematics*, Vol. 52, No. 3, 1994, pp. 297–308.
doi:10.1093/imamat/52.3.297
[20] Baginski, F., Barg, M., and Collier, W., "Existence Theorems for Tendon Reinforced Thin Wrinkled Membranes Subjected to a Hydrostatic Pressure," *Mathematics and Mechanics of Solids*, Vol. 13, No. 6, 2008, pp. 532–570.
doi:10.1177/1081286507077256
[21] Baginski, F., Brakke, K., and Schur, W., "Unstable Cyclically Symmetric and Stable Asymmetric Pumpkin Balloon Configurations," *Journal of Aircraft*, Vol. 44, No. 3, 2007, pp. 764–772.
doi:10.2514/1.20874
[22] Baginski, F., Brakke, K., and Schur, W., "Cleft Formation in Pumpkin Balloons," *Advances in Space Research*, Vol. 37, No. 11, 2006, pp. 2070–2081.
doi:10.1016/j.asr.2005.04.104
[23] Baginski, F., and Brakke, K., "Simulating Clefts in Pumpkin Balloons," *Advances in Space Research*, Vol. 45, No. 4, 2010, pp. 473–481.
doi:10.1016/j.asr.2009.10.022
[24] Berger, M. S., *Nonlinearity and Functional Analysis*, Academic Press, New York, 1977.
[25] Hale, J. K., and Chow, S.-N., *Methods of Bifurcation Theory*, Springer–Verlag, New York, 1982.
[26] Baginski, F., and Brakke, K., "Modeling Ascent Configurations of Strained High-Altitude Balloons," *AIAA Journal*, Vol. 36, No. 10, 1998, pp. 1901–1910.
doi:10.2514/2.284
[27] Clark, I. G., Hutchings, A. L., Tanner, C. L., and Braun, R. D., "Supersonic Inflatable Aerodynamic Decelerators for Use on Future Robotic Missions to Mars," *Journal of Spacecraft and Rockets*, Vol. 46, No. 2, 2009, pp. 340–352.
doi:10.2514/1.38562
[28] Tanner, C. L., Cruz, J. R., and Braun, R. D., "Structural Verification and Modeling of a Tension Cone Inflatable Aerodynamic Decelerator," 51st AIAA/ASME/ASCE/AHS/ASC Structures, Structural Dynamics, and Materials Conference, Orlando, FL, AIAA Paper 2010-2830, 15–20 April 2010.